Korean J. Chem. Eng., 33(12), 3516-3522 (2016)
DOI: 10.1007/s11814-016-0319-8

pISSN: 0256-1115
eISSN: 1975-7220

Iron oxide grown by low-temperature atomic layer deposition

Seenivasan Selvaraj*, Hee Moon*, Ju-Young Yun, and Do-Heyoung Kim*,†**

*School of Chemical Engineering, Chonnam National University, 300 Youngbong-dong, Gwangju 61186, Korea
**Center for Vacuum, Korea Research Institute of Standards and Science, 267 Gajeong-ro, Daejeon 34113, Korea
(*Received 22 October 2016 • accepted 12 November 2016*)

Abstract−Atomic layer deposition (ALD) is a promising technology for fabricating conformal thin films of atom-level thickness with chemical composition control over a variety of structures. This paper demonstrates the ALD of iron oxide thin films using a novel iron precursor, namely, bis[bis(trimethylsilyl)amide]iron [$Fe(btmsa)_2$] and hydrogen peroxide as an oxygen source. The growth characteristics of iron oxide were investigated by varying the deposition temperatures from 100 to 225 °C, such that the ALD growth mode was observed at 150 to 175 °C with an average growth rate of 0.035±0.005 nm/cycle. The films deposited in ALD mode exhibited highly linear film thicknesses with the number of cycles and excellent conformality over high-aspect-ratio trenches. In addition, the deposited films were extremely pure and revealed a hematite phase without any subsequent heat treatment, even if the films were deposited at low temperatures.

Keywords: Atomic Layer Deposition, Precursor, Bis[bis(trimethylsilyl)amide]iron, Hematite, Thin Film, Iron Oxide

INTRODUCTION

Iron is the fourth most abundant element in the Earth's crust. One of its stable natural forms is hematite (α-Fe_2O_3) which has been profoundly analyzed and adopted for a diverse range of applications. Thin films and nanostructures of α-Fe_2O_3 are attracting considerable attention because of their unique intrinsic properties, such as super magnetism, bio-compatibility, UV absorption, and sensitivity compared to bulk structures. In the last decade, thin-film α-Fe_2O_3 has been adopted for a variety of applications, including semiconductors, sensors, catalysts, and solar water splitting, as well as energy, electrical, and magnetic devices [1-5]. To further increase the performance of these devices and commercialize them, it is essential to ensure the properties of the prepared α-Fe_2O_3 thin films by selecting the appropriate deposition technique and source chemicals. Conventionally, α-Fe_2O_3 thin films have being prepared by commercial techniques like sputtering, sol-gel, chemical bath deposition, pyrolysis, chemical vapor deposition (CVD), and atomic layer deposition (ALD) [6-14]. The aforementioned techniques are unable to provide strict control over the properties of thin films, which is imperative for the greater integration of devices, excluding the robust ALD technique [15,16]. ALD is a well-known gas-phase process for producing pin-hole-free conformal thin films of pure metals, oxides, nitrides, and sulfides over a variety of structures [17]. The critical advantages of atom-level thickness, composition control, and self-limiting sequential reactions make ALD a promising candidate for new-generation thin-film formation. This layer-by-layer technique consists of four steps for each ALD cycle: the high-vacuum pulsing of vapor metal compounds which chemically adsorb onto the substrate, the pulsing of a co-reactant known as the oxygen source, and the purging steps between each pulsing for removing excess reactants and by-products. The oxygen source combines with the previously adsorbed metal compound ligands and forms metal-oxide films [18]. Only a few iron-based metal compounds (hereafter, "precursors") were reported for the α-Fe_2O_3 ALD film formation described in Table 1. Ozone (O_3) combined with ferrocene [$Fe(cp)_2$] was the most popular commercial precursor used for α-Fe_2O_3 film formation [19-21]. However, the expense of maintaining an O_3 generator and the necessary high deposition temperatures hinders the wide application of ferrocene. By using bis(2,4-dimethylpentadienyl)iron [$Fe(2,4\text{-}C_7H_{11})_2$], the crystalline phase of the film can be tuned by altering the oxygen source [22]. Even though it offers the pronounced benefit of a low deposition temperature and phase tuning, it relies on O_3 to grow the α-Fe_2O_3 phase. As ozone is a strong oxidizer, it can produce the oxygen-rich α-Fe_2O_3 phase but, as mentioned above, it cannot be economically scaled up. Subsequently, ferric chloride [$FeCl_3$], a highly reactive water-based iron precursor, was reported as being a suitable alternate to O_3. Nevertheless, its application is hampered by its tendency to lead to inimical corrosion issues in the ALD chamber and pumping units on account their coming into contact with Cl and H_2O [23]. Another water-based precursor, bisamidinates, was developed by Gordon et al., and recently the ALD film growth of α-Fe_2O_3 using bis(N,N′-di-t-butylacetamidinato)iron(II) [FeAMD]/H_2O at low temperatures was attempted by Avila et al. [24,25]. The low vapor pressure of FeAMD gives rise to a need for a sufficiently long interval between each pulse to confirm the uniform precursor delivery in each cycle. Furthermore, other precursors such as [$Fe(thd)_3$] and [$Fe_2(O^tBu)_6$] are plagued by a low growth rate and slow nucleation mechanisms [26-28]. Therefore, to overcome the problems associated with the aforementioned precursors, the identification of a new precursor is essential to the preparation of a phase-pure α-Fe_2O_3

†To whom correspondence should be addressed.
E-mail: kdhh@chonnam.ac.kr

Table 1. Iron precursors and ALD conditions for iron oxide film growth (from the literature)

S. no	Precursor	Oxygen source	Deposition temperature (°C)	Growth rate (nm/cycle)	Crystalline phase	Reference
1	$Fe(Cp)_2$	O_2	360-530	0.015	Mixed	19,21
2	$Fe(Cp)_2$	O_3	170-350	0.14	α-Fe_2O_3	20
3	$FeCl_3$	H_2O	200-350	0.06	α-Fe_2O_3	23
4	$Fe(2,4\text{-}C_7H_{11})_2$	H_2O_2	120	0.06	Fe_3O_4	22
5	$Fe(2,4\text{-}C_7H_{11})_2$	O_3	120	0.06	α-Fe_2O_3	22
6	FeAMD	H_2O	130-200	0.055	α-Fe_2O_3	25
7	$Fe(thd)_3$	O_3	160-210	0.01	α-Fe_2O_3	26
8	$Fe_2(O^tBu)_6$	H_2O	130-170	0.026	-	27
9	$Fe(acac)_3$	O_2	180	-	-	28

film under relatively mild conditions, such as the use of low temperatures and smooth oxidizers. From a practical point of view, low temperature ALD process is desirable because it allows energy saving as well as a wider choice of substrate materials including thermally fragile organics and polymers. Any such system should incorporate clean chemistry, mild deposition conditions, and phase purity in addition to the advantage of using moderate, cheap oxidizers like H_2O or H_2O_2. In this respect, we are introducing a novel amide precursor that offers the potential to grow a range of transition metal-oxide films under mild conditions with clean chemistry [29]. We use bis(bis(trimethylsilyl)amide) iron(II) [$Fe(btmsa)_2$] and H_2O_2 to grow α-Fe_2O_3 at relatively low deposition temperatures, which we then go on to compare with other iron precursors. The chemical structure of $Fe(btmsa)_2$ is shown in Fig. 1. To the best of our knowledge, there have been no reports published describing the use of this amide precursor for growing ALD transition metal-oxide films. In general, the crystallinity of the ALD-grown films depends on the deposition temperature (relatively high), subsequent heat treatments, or the oxygen source [23,25,30]. An intriguing fact regarding [$Fe(btmsa)_2$]/H_2O_2 is that the as-deposited films become crystalline once the required thickness is attained [20,22]. In this study, we set out to elucidate the salient benefits of the [$Fe(btmsa)_2$]/H_2O_2 ALD system for the fabrication of pure α-Fe_2O_3 thin films.

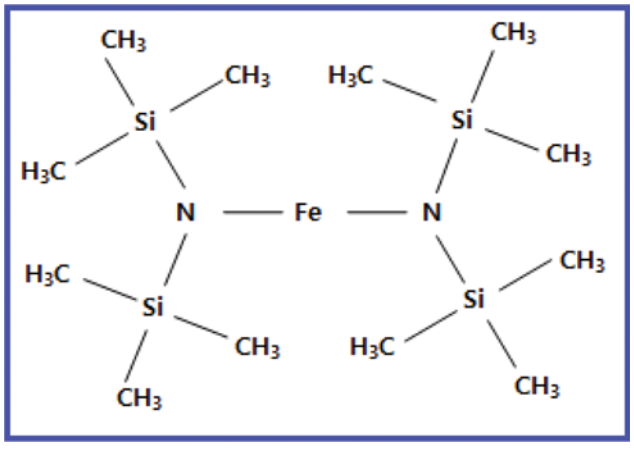

Fig. 1. The chemical structure of $Fe(btmsa)_2$.

EXPERIMENT

1. Materials

All experiments were carried out in a horizontal-flow reactor, fabricated in house, with a chamber diameter of 35 mm and a length of 380 mm, positioned inside a tubular furnace to avoid temperature profiling. $Fe(btmsa)_2$ (Hansol Chemical, Korea) and 30-wt% H_2O_2 (Sigma Aldrich, USA) were alternatively pulsed to form α-Fe_2O_3 film. We used 99.99% pure compressed argon (Praxair, USA) as both a carrier (20 sccm) and purge (50 sccm) gas. Single-crystalline p-type silica (100) substrates (LG Siltron, Korea) were thoroughly dip-cleaned with diluted hydrofluoric acid for 60-120 s to remove the natural SiO_2 layers. Prior to being blown dry with 99.99% pure nitrogen (Praxair, USA) the substrates were rinsed first with acetone, then isopropanol, and finally distilled water for a few minutes.

2. Method

The effects of temperature on the growth mechanism were examined by examining the deposition over a wide range of temperatures from 100 to 225 °C. For every deposition, a base pressure of 800 mTorr was maintained by means of a high-purity Ar flow at a mass flow rate of 50 sccm. The iron precursor bubbler was maintained at 65 °C to create sufficient vapor to uniformly deliver the precursor, even over a large number of cycles. The H_2O_2 bubbler and gas/vapor lines were maintained at 35 °C and 90 °C, respectively, to prevent condensation of the precursor. The precursor line consists of a mixing zone and a reservoir. The mixing zone facilitates the proper mixing of the carrier gas and precursor vapor cloud by forcing the carrier gas (20 sccm) into the mixing zone. Arresting the mixed-vapor phase (carrier gas and precursor vapor) in the reservoir for a short time prior to pulsing prevents any direct/excess flow from the bubbler and ensures uniform precursor delivery in each cycle. The hydrogen peroxide line featured only a reservoir because no carrier gas was utilized. The ALD cycle sequences are generally denoted as t1-t2-t3-t4, where t1 is the pulsing time of the precursor, t2 is the purge-out time for excess precursor, t3 is the pulsing time of the oxygen source, and t4 is the purge-out time for any excess oxygen source and by-products. The self-limiting nature of each half-reaction was examined by altering the pulsing (t1 & t3) and purging (t2 & t4) times. All the cycle sequence timings were accurately controlled by pneumatic valves. A distance-inde-

pendent regime was found between 5 and 22 cm from the precursor inlet [20]. The growth rate starts to fall after 22 cm because of the concentration gradient. All the experimental data shown hereafter correspond to the distance-independent regime. At the end of all the experiments, the samples were outgassed with 50 sccm Ar for 60 s. For the chosen samples, annealing in an air atmosphere was carried out in a box furnace at 550 °C with a heating rate of 5 °C/min for 4 h, after which they were allowed to cool naturally.

3. Characterization

The thicknesses of the ALD-grown films were measured using an LSE Stokes ellipsometer (Gaertner Scientific, USA) using a low-power HeNe (632.8-nm) measurement laser beam. The crystallinity of the films was observed by means of grazing incidence X-ray diffraction (GIXRD) using an Empyrean diffractometer (PANalytical, the Netherlands) using a Cu Kα radiation and a pixcel3D detector with a prefix interface. The incident angle used was 1° and the 2θ range was 20 to 80°. In addition, X-ray photoelectron spectroscopy (XPS) was performed using a VG Multilab 2000 (Hosmed, Finland) with a 7-channeltron detector was used to analyze the film composition and chemical oxidation states of the elements present in the film. Atomic force microscopy (XE-100) was employed in noncontact mode for the surface roughness measurements. The surface morphologies of the silica substrates were examined through field emission scanning electron microscopy (FE-SEM) using an S-4700 microscope (Hitachi, Japan).

RESULTS AND DISCUSSION

First, films were grown on flat Si(100) substrates by using alternating pulses of $Fe(btmsa)_2$ and H_2O_2 vapors at 100 °C. In each cycle, the H_2O_2 reacted with the chemisorbed $Fe(btmsa)_2$ species. The deposition temperature is paramount for achieving true ALD behavior since the adsorption and kinetics of the reactions rely greatly on the vapor phase and substrate temperature. The ALD window, a brief temperature range in which self-limiting half-cycle reactions occur without any CVD component, is essential to the definition of any ALD system [15]. We carried out the deposition between 100 °C over 300 cycles and a cycle sequence of 1.5 s-20 s-0.5 s-55 s to define the ALD window for an $Fe(btmsa)_2/H_2O_2$ system. Fig. 2(a) shows the growth rate as a function of temperature. As shown in Fig. 2, the growth rate of Fe_2O_3 ALD is slower than those of other metal oxides ALD such as TiO_2 and ZnO [15]. In general, chemisorbed precursors should react rapidly with a counter reactant to obtain a high growth rate and thus, it can be presumed that the slow growth rate of the Fe_2O_3 ALD is caused by the absent of the aggressive reactions between $Fe(btmsa)_2$ and H_2O_2. Nevertheless we can see the true ALD behavior at a significantly low temperature range of 150 to 175 °C. The slight slope indicates that the film growth is affected by the substrate temperature within the ALD window. The higher growth rate observed below 150 °C is ascribed to the $Fe(btmsa)_2$ condensations on the substrates. On the other hand, the film growth rate is decreased with increased deposition temperatures above 175 °C, due to the enhanced desorption of the adsorbed precursors from the surfaces [15]. Attempts to form films at a higher temperature of around 225 °C generate rough films in contradiction to the ALD window. Through AFM

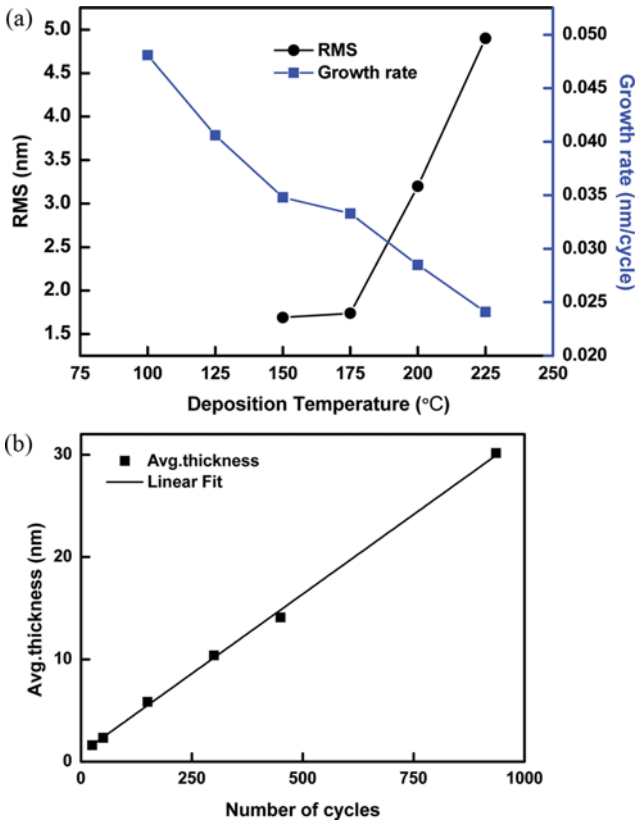

Fig. 2. (a) Growth rate as a function of deposition temperature, (b) Film thickness measured by ellipsometry (solid square) versus number of ALD cycles.

analysis (not described in this paper), the roughness was found to be 1.74 and 4.90 nm for the films grown at 175 °C and 225 °C respectively, with the same cycle sequence (1.5 s-20 s-0.4 s-60 s) and number of cycles. The size of the crystals at high deposition temperatures was relatively large, which gives rise to the relatively rough surface [31]. The uncontrolled and rapid decomposition of the precursor might be the reason for this phenomenon. From these features, we can conclude that 150-175 °C is the optimum ALD window for an $Fe(btmsa)_2/H_2O_2$ system. Fig. 2(b) shows the linear relationship between the film thickness and number of cycles at 150 °C for a cycle sequence of 1.5 s-20 s-0.4 s-60 s. There was no evidence of nucleation delay. The positive intercept of the linear fitting curve (0.9) is caused by the presence of an unsteady state in the initial cycles. A higher growth rate was witnessed in the initial cycles (up to 50) which can be neglected as an instrumentation error. In every experiment, the precursor delivery reached the steady state after 50 cycles and did not have any noticeable effect on the growth mechanism for a high number of cycles. After defining the ALD window, the self-limiting kinetics were verified with different pulse and purge sequences. The individual half-reaction saturation is essential to a true ALD process. If the purging is not adequate, then the ALD system will fail in terms of either the multilayer formation or CVD components. Identifying the optimum self-limiting cycle sequence is essential to the fabrication of conformal smooth films. We started to investigate the pulsing steps (t1 & t3) while t3 and t4 were held constant to prevent any intrusion.

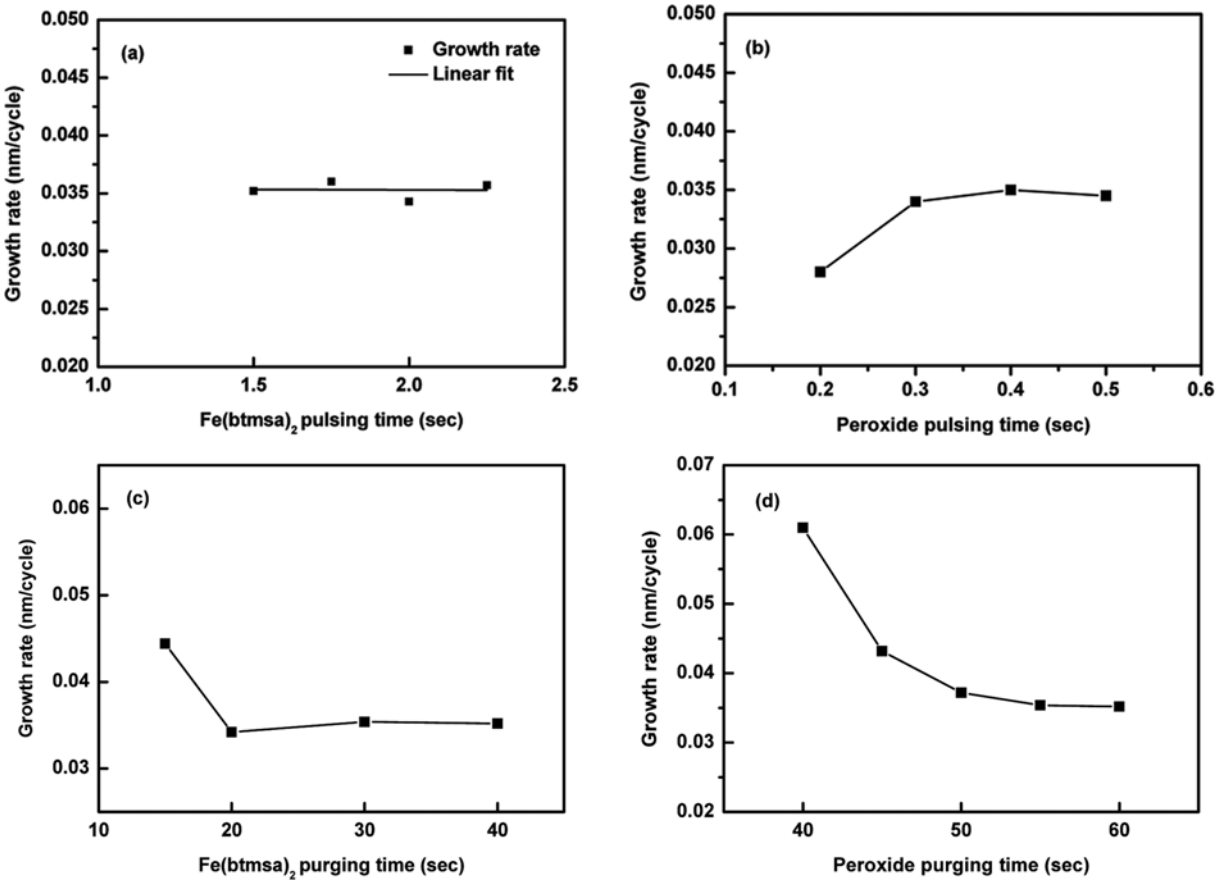

Fig. 3. Effect of (a) precursor pulsing time, (b) oxygen source pulsing time, (c) precursor purging time and (d) oxygen source purging time on film growth rate at 150 °C.

$Fe(btmsa)_2$ pulsing (t1-20 s-0.4 s-60 s) was varied from 1 to 2.25 s. Surprisingly, not even a very slight slope was observed with the relation fit. Briefly, a surface that has been saturated with 1-s and longer pulses has no effect on the monolayer formation, as shown in Fig. 3(a). $Fe(btmsa)_2$ appears to be superior to ferrocene since a pulse of at least 30 s and a long purge were needed to attain saturation and true ALD [20]. Saturation was also observed beyond the bounds of the ALD window, even though the growth rate varied, as shown in Fig. 2(a). A significant advantage of an $Fe(btmsa)_2$/H_2O_2 system is that the ALD window can be drawn out to lower temperatures for certain applications. An examination of H_2O_2 pulsing (1.5 s-20 s-t3-60 s) revealed surface saturation at 0.4 s. There was a gradual increase in the growth rate from 0.2 to 0.4 s, after which the growth rate was independent of the pulse time, as depicted in Fig. 3(b). H_2O_2 is a stronger oxidizer than molecular water and very comparable to an O_3/O_2 mixture, making its use preferable to O_3 when scaling-up the process. In the case of purging, a sufficiently long purge-out duration is essential to avoid the incorporation of CVD components into the films. Doing so also helps to ensure the surface saturation. Using the cycle sequence 1.5 s-t2-0.4 s-t4, the purging effects of both half-cycles were examined, and it was found that 20 s for t2 and 55 s for t4 was sufficient to confirm the monolayer formation, as shown in Fig. 3(c) and 3(d). A duration in excess of this does not have any noticeable effect on the growth rate. Even very long purge times, such as 50 s for t2 and 120 s for t4, could not resolve the multilayer formation near the inlet portion (0-5 cm) of the tubular ALD reactor. This may be due to either of two causes: (1) vapor turbulence or hindrance near the inlet, or (2) the concentration gradient of the precursor in the chamber. Finally, the growth rate was found to be 0.035±0.005 nm/cycle, using the ellipsometry thickness data in the true ALD distance-independent regime without any nucleation delay.

For phase identification, chosen samples coated under different deposition conditions were subjected to grazing-incidence XRD analysis. The diffraction patterns were compared with the standard patterns to confirm the phase purity and crystallinity of the formed films. Those films with a thickness of less than 25 nm did not exhibit any diffraction peaks, thus confirming that the films were amorphous regardless of the deposition temperature (blue spectra in Fig. 4). No crystallinity could be observed in the same samples, even after air annealing at 550 °C. The diffraction peaks of the films deposited at 150 °C, about 30 nm thicker, exhibit a pure α-Fe_2O_3 phase without any additional phases (black spectra in Fig. 4). This is in contrast to the $FeCl_3/H_2O$ and $Fe(cp)_2/O_2$ systems where they exhibit a mixture of α-Fe_2O_3 and Fe_3O_4 at relatively higher deposition temperatures [21,23]. The green spectral line in Fig. 4 indicates the diffraction peaks of the annealed samples, revealing a very high crystallinity and phase purity where the high-intensity peaks per-

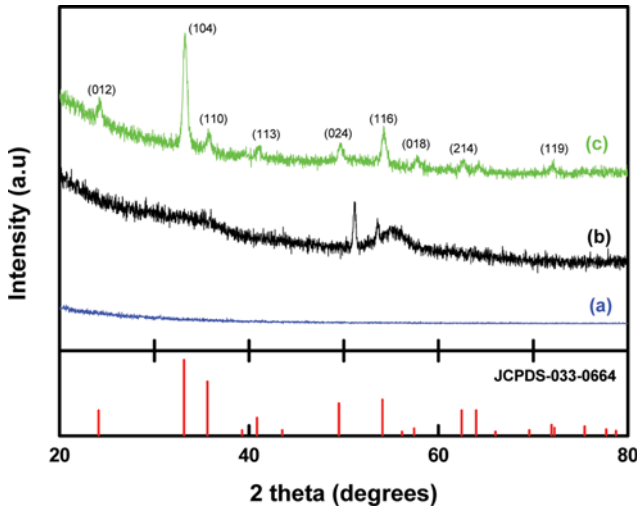

Fig. 4. GIXRD data for films grown on Si(100) at 150 °C. (a) 10 nm, (b) 30 nm (c) 30 nm film annealed at 550 °C.

fectly match the reference pattern (JCPDS 033-0664). In normal cases, the deposition temperature, post treatments, and choice of oxygen source are crucial to the determination of the phase and chemical composition of an ALD film. For example, the use of $Fe(2,4\text{-}C_7H_{11})_2$ prevents the mixing of Fe_3O_4 and pure α-Fe_2O_3, while using H_2O_2 and O_3 as the oxygen source, respectively [22]. When deriving α-Fe_2O_3, highly oxidative sources like O_3 or high-temperature post treatments are essential when using known precursors. Nevertheless, in the case of $Fe(btmsa)_2$, the use of H_2O_2 is sufficient to produce phase-pure α-Fe_2O_3 thin films even at low deposition temperatures in the absence of post heat treatments.

Further surface-oriented X-ray photoelectron spectroscopy was applied to further confirm the chemical composition of α-Fe_2O_3 films. A 30-nm sample, deposited at 150 °C with a cycle sequence of 1.5 s-20 s-0.5 s-60 s was analyzed and no trace elements other than Fe, O, and C were observed in the full XPS analysis function, as illustrated in Fig. 5(a). Fig. 5(b) indicates that the C1s profile contains a highly intense (284.9 eV) and two less-intense (287.4 eV, 289.7 eV) peaks that can be attributed to the C-C, C-OH, and C=O (hydrocarbons) structures, respectively [32,33]. The quantitative carbon content is 0.059 at% in a 30-nm film, which may result from the presence of undesirable precursor decomposition products. Post thermal or plasma treatment may further reduce the level of the carbon impurities in the films [34].

As shown in Fig. 5(c) the O1s also contains three peaks. Among these, the higher, most-intense peak (530.4 eV) corresponds to the fundamental metal-oxygen (Fe-O) bonding. Among the two less-intense peaks, the first (531.8 eV) corresponds to the oxygen-containing hydrocarbons and general defects, while the second (532.7 eV) stems from the natural SiO_2 layers formed over the Si(100)

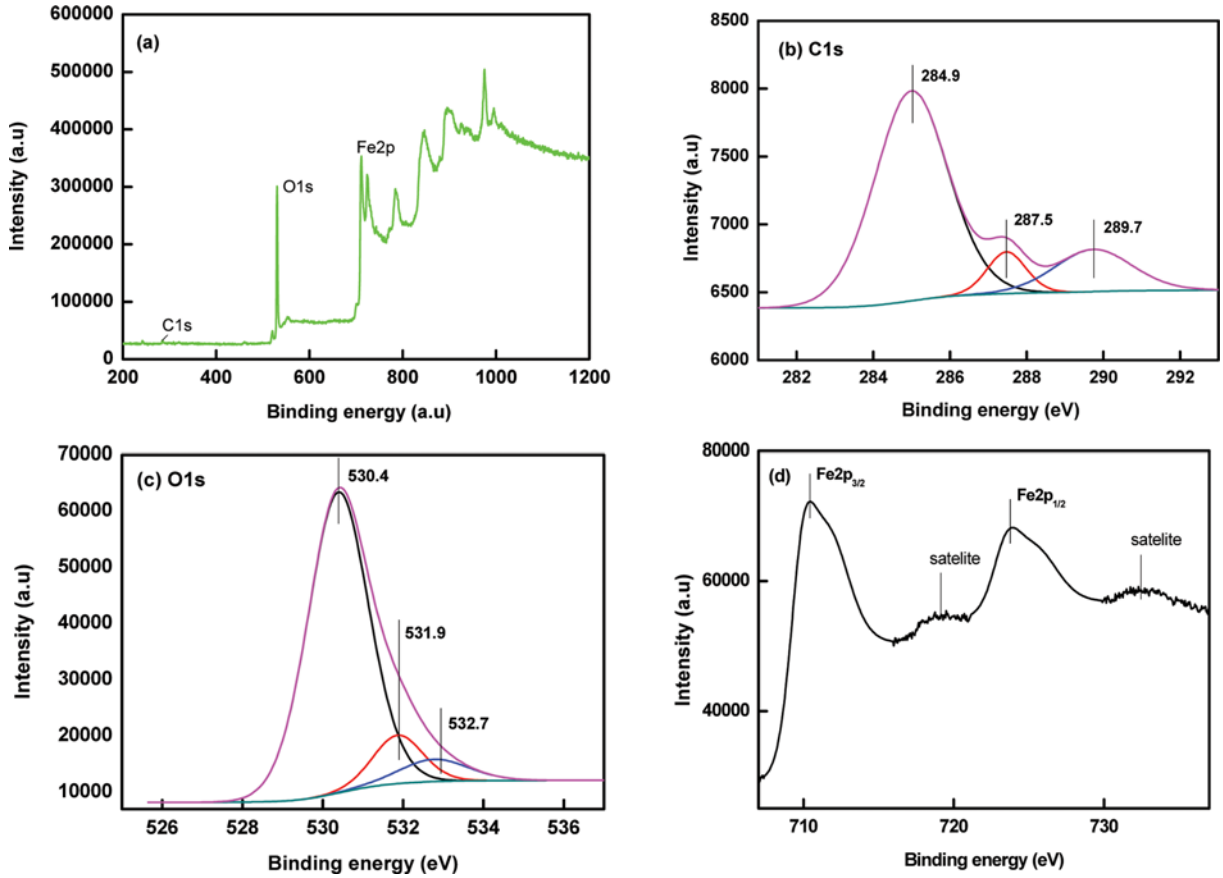

Fig. 5. XPS spectra of film deposited at 150 °C. (a) Wide spectra, (b) C1s, (c) O1s, and (d) Fe2p.

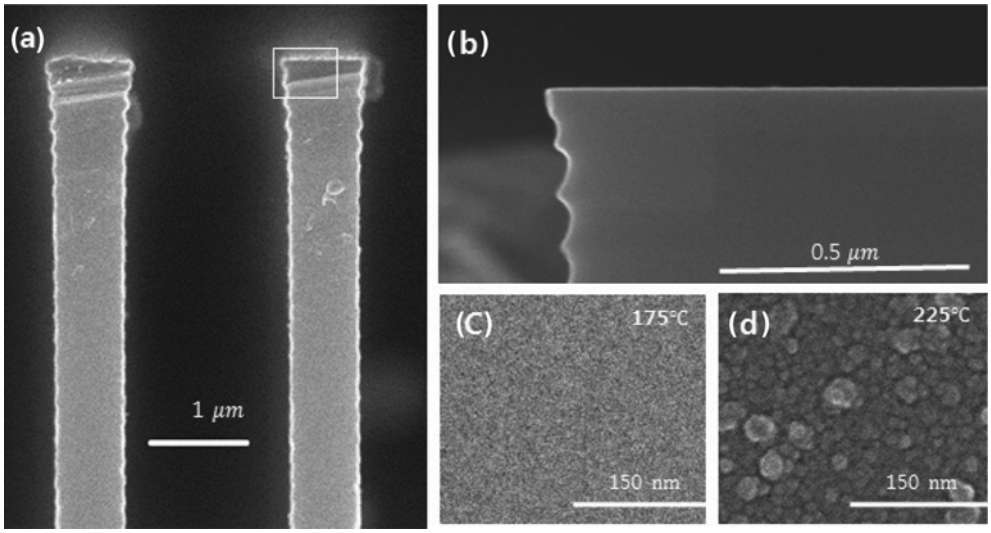

Fig. 6. (a) Cross section SEM micrograph of film deposited on patterned Si(100) substrate at 150 °C, (b) enlarged view of marked portion in (a), (c) top view of film deposited on flat Si(100) substrate at 175 °C, (d) at 225 °C.

substrates [33]. Fig. 5(d) shows the detailed spectrum of the Fe2p regime with two spin-orbit-coupling energy states $2p_{3/2}$ and $2p_{1/2}$, with a splitting energy of 13.45 eV. The corresponding energy levels of the $2p_{3/2}$ and $2p_{1/2}$ peaks are 710.5 and 723.9 eV, respectively. Furthermore, two satellite peaks were located around 718.2 and 728.8 eV, corresponding to the $2p_{3/2}$ and $2p_{1/2}$ main peaks. The spectral data and peak positions are identical to the previously reported XPS spectra of pure α-Fe_2O_3 [35,36]. Both X-ray analysis techniques confirmed that only the α-Fe_2O_3 phase is present in the film, rather than a missed phase.

The ability to fabricate conformal films over high-aspect-ratio structures is vital to the commercialization of ALD systems. Therefore, the conformality of the films grown with the Fe(btmsa)$_2$/H_2O_2 system was examined using patterned Si(100) substrates with an aspect ratio of 10. The substrates were coated over 300 cycles with a 1.5 s-20 s-0.4 s-60 s sequence at 150 °C. The SEM micrograph of the cross-section, shown in Fig. 6(a), and the magnified edge portion, shown in Fig. 6(b), evidence a continuous uniform film over all the intricate surfaces of the substrate. From the AFM analysis, it was acknowledged that the roughness increases with the deposition temperatures. The SEM micrographs shown in Fig. 6(c) and (d) support this statement. Larger crystals/particles are visible on the substrate coated at 250 °C. In contrast, the substrate coated at 175 °C has a smooth surface. This paper thus explains the intriguing and appreciable advantages of an Fe(btmsa)$_2$/H_2O_2 system over other available iron precursors in terms of growth conditions, clean chemistry, and film quality. Further investigation of the α-Fe_2O_3 thin film for application as a light-harvesting photo anode for solar water splitting is ongoing.

CONCLUSION

The self-limiting ALD of pure α-Fe_2O_3 has been demonstrated using a novel metal precursor, namely, bis[bis(trimethylsilyl)amide] iron, under undemanding conditions. Alternate pulsing of Fe(btmsa)$_2$ and H_2O_2 resulted in a normalized growth rate of 0.035±0.005 nm/cycle. The as-deposited films exhibit satisfactory crystallinity regardless of the post treatment, deposition temperature, and extreme oxidizers. Despite being cheap and only a moderate oxidizer, H_2O_2 is ample for deriving phase-pure α-Fe_2O_3 without any other phases through an Fe(btmsa)$_2$/H_2O_2 system. The phase purity is established through GIXRD and XPS analyses. The dynamic capability to fabricate crystalline thin films under relatively undemanding growth conditions, the clean surface chemistry, and potential make the Fe(btmsa)$_2$/H_2O_2 ALD system a promising candidate for the fabrication of phase-pure α-Fe_2O_3 thin films.

REFERENCES

1. A. G. Tamirat, J. Rick, A. A. Dubale, W. N. Su and B. J. Hwang, *Nanoscale Horiz.*, **1**(4), 243 (2016).
2. P. Tartaj, M. P. Morales, T. G. Carreno, S. V. Verdaguer and C. J. Serna, *Adv. Mater.*, **23**(44), 5243 (2011).
3. T. Hisatomi, H. Dotan, M. Stefik, K. Sivula, A. Rothschild, M. Gratzel and N. Mathews, *Adv. Mater.*, **24**(20), 2699 (2012).
4. H. I. Adegoke, F. AmooAdekola, O. S. Fatoki and B. J. Ximba, *Korean J. Chem. Eng.*, **31**(1), 142 (2014).
5. X. Lu, Y. Zeng, M. Yu, T. Zhai, C. Liang, S. Xie, M. S. Balogun and Y. Tong, *Adv. Mater.*, **26**(19), 3148 (2014).
6. K. Siroky, J. Jireova and L. Hudec, *Thin Solid Films*, **245**, 211 (1994).
7. L. Huo, Q. Li, H. Zhao, L. Yu, S. Gao and J. Zhao, *Sens. Actuators B*, **107**(2), 915 (2005).
8. G. Neri, A. Bonavita, S. Galvagno, Y. X. Li, K. Galatsis and W. Wlodarski, *IEEE Sens. J.*, **3**, 195 (2003).
9. A. Duret and M. Gra1tzel, *J. Phys. Chem. B.*, **109**(36), 17184 (2005).
10. M. Cornuz, M. Gratzel and K. Sivula, *Chem. Vap. Deposition*, **16**(10-12), 291 (2010).
11. G. Carraro, A. Gasparotto, C. Maccato, E. Bontempi and D. Barreca, *Chem. Vap. Deposition*, **21**(10-12), 291 (2005).

12. Y. Lin, Y. Xu, M. T. Mayer, Z. I. Simpson, G. McMahon, S. Zhou and D. Wang, *J. Am. Chem. Soc.*, **134**(12), 5508 (2012).
13. S. C. Riha, B. M. Klahr, E. C. Tyo, S. Seifert, S. Vajda, M. J. Pellin, T. W. Hamann and A. B. F. Martinson, *ACS Nano.*, **7**(3), 2396 (2013).
14. O. Zandi, B. M. Klahr and T. W. Hamann, *Energy Environ. Sci.*, **6**(2), 634 (2013).
15. S. M. George, *Chem. Rev.*, **110**(1), 111 (2010).
16. S. H. Lim, S. W. Seo, H. Lee, H. Chae and S. M. Cho, *Korean J. Chem. Eng.*, **33**(6), 1971 (2016).
17. M. Knez, K. Nielsch and L. Niinisto, *Adv. Mater.*, **19**(21), 3425 (2007).
18. V. Miikkulainen, M. Leskela, M. Ritala and R. L. Puurunen, *J. Appl. Phys.*, **113**, 021301 (2013).
19. J. R. Scheffe, A. Frances, D. M. King and X. Liang, *Thin Solid Films*, **517**(6), 1874 (2009).
20. A. B. F. Martinson, M. J. Devries, J. A. Libera, S. T. Christensen, J. T. Hupp, M. J. Pellin and J. W. Elam, *J. Phys. Chem. C.*, **115**(10), 4333 (2011).
21. M. Rooth, A. Johansson, K. Kukli, J. Aarik, M. Boman and A. Harsta, *Chem. Vap. Deposition*, **14**(3-4), 67 (2008).
22. S. C. Riha, J. M. Racowski, M. P. Lanci, J. A. Klug, A. S. Hock and A. B. F. Martinson, *Langmuir*, **29**(10), 3439 (2013).
23. J. A. Klug, N. G. Becker, S. C. Riha and A. B. F. Martinson, *J. Mater. Chem. A.*, **1**, 11607 (2013).
24. B. S. Lim, A. Rahtu and R. G. Gordon, *Nature Mater.*, **2**, 749 (2003).
25. J. R. Avila, D. W. Kim, M. Rimoldi and O. K. Farha, *ACS Appl. Mater. Interfaces*, **7**(30), 16138 (2015).
26. M. Lie, H. Fjellvag and A. Kjekshus, *Thin Solid Films*, **488**(1-2), 74 (2005).
27. J. Bachmann, J. Jing, M. Knez, S. Barth, H. Shen, S. Mathur, U. Gosele and K. Nielsch, *J. Am. Chem. Soc.*, **129**(31), 9554 (2007).
28. M. de Ridder, P. C. van de Ven, R. G. van Welzenis, H. H. Brongersma, S. Helfensteyn, C. Creemers, P. V. D. Voort, M. Baltes, M. Mathieu and E. F. Vansant, *J. Phys. Chem. B,* **106**(51), 13146 (2002).
29. R. A. Andersen, K. Faegri Jr., J. C. Green, A. Haaland, M. F. Lappert, W. P. Leung and K. Rypdal, *Inorg. Chem.*, **27**(10), 1782 (1988).
30. J. A. Libera, J. N. Hryn and J. W. Elam, *Chem. Mater.*, **23**(8), 2150 (2011).
31. D. M. Hausmann and R. G. Gordon, *J. Crystal Growth*, **249**, 251 (2003).
32. B. Sambandam, A. Surenjan, L. Philip and T. Pradeep, *ACS Sustainable Chem. Eng.*, **3**(7), 1321 (2015).
33. S. Karakalos, A. Siokou and S. Ladas, *Appl. Surf. Sci.*, **255**(21), 8941 (2009).
34. D.-H. Kim, J. J. Kim, J. W. Park and J. J. Kim, *J. Electrochem. Soc.*, **143**(9), L188 (1999).
35. N. S. McIntyre and D. G. Zetaruk, *Anal. Chem.*, **49**(11), 1521 (1977).
36. A. P. Grosvenor, B. A. Kobe, M. C. Biesinger and N. S. McIntyre, *Surf. Interface Anal.*, **36**(12), 1564 (2004).